Journal of Nuclear Materials xxx (xxxx) 154787

Contents lists available at ScienceDirect

Journal of Nuclear Materials

journal homepage: www.elsevier.com/locate/jnucmat

Structural features of early fuel cycle taggant incorporation for intentional nuclear forensics

Tyler L. Spano [a, *], Toya Beiswenger [a], Benjamin T. Manard [c], Tash L. Ulrich [b], Rodney Hunt [b], Andrew Miskowiec [a], Ashley E. Shields [a]

[a] Nuclear Nonproliferation Division, Oak Ridge National Laboratory, Oak Ridge, TN, United States
[b] Nuclear Energy and Fuel Cycle Division, Oak Ridge National Laboratory, Oak Ridge, TN, United States
[c] Chemical Sciences Division, Oak Ridge National Laboratory, Oak Ridge, TN, United States

ARTICLE INFO

Article history:
Received 2 August 2023
Received in revised form 12 October 2023
Accepted 16 October 2023

Keywords:
Nuclear forensics
Uranyl nitrate
Uranyl peroxide
Studtite
Metastudtite
Raman spectroscopy

ABSTRACT

To develop strategies for incorporating transition metal taggants (Fe, Cr, and Ni) into oxide fuels and to understand how these taggant candidates persist through early fuel cycle processes, synthetic procedures are modified from established production routes to yield intentionally tagged early fuel cycle intermediates including uranyl nitrate hexahydrate (UNH, $UO_2(NO_3)_2{\cdot}6H_2O$), uranyl peroxide tetrahydrate (studtite, $UO_2O_2{\cdot}4H_2O$), and uranyl peroxide dihydrate (metastudtite, $UO_2O_2{\cdot}2H_2O$). First, Fe, Cr, and Ni nitrate solutions are introduced to an aqueous solution of UNH followed by precipitation to produce tagged UNH. Then, studtite is precipitated from UNH followed by dehydration to metastudtite. Structural influences of taggant incorporation within all synthesized phases are investigated using powder X-ray diffraction (PXRD) and Raman spectroscopy to provide insight into crystallographic modifications resulting from the addition of tags to these early fuel cycle materials and elucidate the chemical form of taggants introduced at these stages. The possibility of segregation of taggant species into discrete phases within U matrices was examined using scanning electron microscopy with energy dispersive X-ray spectroscopy. Taggant concentrations in solid-phase materials were determined using inductively coupled plasma-optical emission spectrometry. Observations from Raman spectroscopy and PXRD indicate that introducing transition metal tags during uranyl nitrate precipitation results in potential impurity phase segregation in UNH, but transition metal incorporation is suggested by results for tagged uranyl peroxide materials. Results from this study will inform strategies for optimizing taggant incorporation in UO_2.

1. Introduction

Rare earth elements (REEs, La through Lu) are well-established as powerful indicators of the provenance of early nuclear fuel cycle materials [1–6]. In particular, the shape of chondrite normalized REE plots are strongly coupled to the geologic deposit type from which uranium ores originate [3,4,7]. In some cases, limited fractionation of REEs is observed during conversion from uranium ore to uranium ore concentrate (UOC), suggesting that this is a viable forensic indicator for provenance assessment of early fuel cycle materials [2,8]. Regarding UO_2 fuel pellets, however, lanthanide contributions to observed trace element signatures are negligible, indicating that beyond enrichment, provenance assessment via REE signature analysis is limited based on previous work [9]. Conversely, transition metal concentrations in fuel pellets with both natural and enriched U isotopic abundances were found to correlate strongly with the geologic deposit type, and specifically, the uranium mine from which the ore originated [9]. The persistence of transition metals throughout ore processing and enrichment as indicated by observation of these phases in sintered UO_2 fuel suggests that elemental concentrations and ratios of Cr, Fe, and Ni, for example, may be valuable indicators of material provenance.

Keegan et al. [2] use transition metal signatures (e.g. Ti and Fe) as characteristic impurities to identify uranium ore concentrate samples based on the geologic deposit type from which they originated. Likewise, during a collaborative exercise to certify a new reference material, anomalous Cr, Fe, and Ni signals attributable to corrosion of storage containers was observed. While the transitional metals measured during this study were characterized as impurities [10], understanding the persistence and potential structural features resulting from incorporation of transition metals in U-rich matrices remains an open question in nuclear forensics literature.

To systematically explore the persistence of transition metals through analysis of products from bench-scale analogs of early fuel cycle processes, we have prepared uranyl nitrate intentionally tagged with Fe, Cr, and Ni and from this starting material, synthesize uranyl peroxide tetra- and di-hydrate (studtite and metastudtite, respectively).

* Corresponding author.
E-mail address: spanotl@ornl.gov (T.L. Spano).

https://doi.org/10.1016/j.jnucmat.2023.154787
0022-3115/© 20XX

This enables a detailed investigation of structural modifications, elemental partitioning, and persistence of these transition metals in U milling and conversion early fuel cycle processes.

2. Materials and methods

2.1. Synthesis

Uranyl nitrate hexahydrate was prepared via slow evaporation. First, a 1 M uranyl nitrate stock solution was prepared by transferring 50.834 g $UO_2(NO_3)_2 \cdot 6H_2O$ to a Nalgene bottle to which 100.48 mL deionized (di) H_2O was added. Taggant solutions were prepared by dissolving 11.5 g $Cr(NO_3)_3 \cdot 9H_2O$ in 57.4 mL di H_2O, 13.258 g $Fe(NO_3)_3 \cdot 9H_2O$ in 49.016 mL di H_2O, and 14.218 g $Ni(NO_3)_2 \cdot 6H_2O$ in 47.086 mL di H_2O, with resulting concentrations of 0.5, 0.7, and 1.0 M, respectively. These concentrations were chosen to ensure that tags would be detectable using scanning electron microscopy with energy dispersive X-ray spectroscopy (SEM-EDS) to investigate the spatial distribution of transition metals in a UNH matrix. Tagged uranyl nitrate solutions were made by combining 20 mL aliquots of uranyl nitrate stock solution with 1 mL of aqueous Cr, Fe, or Ni-nitrate solutions resulting in 21 mL of tagged uranyl nitrate solutions. An additional 20 mL aliquot of untagged (blank) uranyl nitrate was prepared simultaneously. Each of the uranyl nitrate solutions were covered with perforated parafilm and allowed to evaporate under ambient conditions resulting in crystalline phases shown in Fig. 1.

Tagged studtite ($UO_2O_2 \cdot 4H_2O$) was synthesized using a method after Burns et al. where 30% H_2O_2 was added dropwise to 1 M uranyl nitrate solutions (described above) resulting in a pale-yellow precipitate [11]. The precipitated studtite was recovered via vacuum filtration and was not washed. Metastudtite ($UO_2O_2 \cdot 2H_2O$) samples were prepared from synthesized studtite by transferring the material to porcelain crucibles and heating at 353 K for 48 h following methods described previously [12].

2.2. Characterization

Synthetized tagged and untagged uranyl nitrate, studtite, and metastudtite were characterized with powder X-ray diffraction (PXRD), Raman spectroscopy, SEM-EDS, and inductively coupled plasma-optical emission spectrometry (ICP-OES). Approximately 50 mg of each sample was combined with NIST 640e line standard and transferred to a zero-background silicon substrate for PXRD analysis. Data were collected with a Proto AXRD benchtop powder diffractometer in Bragg-Brentano configuration. The samples were illuminated with a Cu–Kα (λ = 1.5406 Å) X-ray source, and data was acquired with a Dectris Mythen 1 K 1D detector equipped with a β- filter. Incident and diffracted beam Soller slits and a 0.2 mm divergence slit were used to reduce axial divergence of the X-ray beam. Data were collected with a step velocity of 0.06° 2θ/min in the range of 10–55° 2θ. Zero shift corrections were performed using the (111), (220), (311), (400), and (331) reflections of NIST 640e.

Raman spectra were collected for UNH, studtite, and metastudtite using a Renishaw inVia™ micro-Raman spectrometer. An excitation wavelength of 785 nm was used to collect data in the range of 35–1000 cm^{-1} in combination with a 1200 lines/mm diffraction grating, resulting in spectral resolution of ~2.5–3.1 cm^{-1} with a holographic notch filter providing spectral sensitivity to 35 cm^{-1}. The resulting power density for Raman measurements is ~100 W/cm^2 based on estimated laser power (10 mW) and spot size (~1 μm[2]). Reported spectra are the sum of 20 accumulations, each with a 10 s exposure time.

A field emission scanning electron microscope (FE-SEM, Zeiss Gemini 460) equipped with two energy dispersive X-ray spectrometers (Bruker) was employed to investigate the spatial distributions of taggants in synthesized samples. This technique gives a detailed view of a samples chemical composition and provides high-resolution images with topographical and elemental contrast information. For this portion of the experiment, particles were dispersed by dusting small quantities of material on a 12 mm aluminum pin mount adhered with a double-sided carbon adhesive tab. To maintain the original sample state, mounts were not coated with C. Our objective is to use elemental maps to determine the distribution of various taggants within synthesized U compounds. To examine the robustness of the samples, the mounts were each initially exposed to an accelerating voltage of 15 kV to determine whether they could withstand the amount of energy without altering or dislodging the position of the particles. Most samples were very fragile and unstable at that higher voltage and had to be analyzed at 10 kV to ensure that no electron beam-induced chemical transformations occurred. While, an acceleration voltage of 10 kV did not provide sufficient energy to adequately excite the U Lα line at 13.614 keV, this voltage was still appropriate for taggant mapping as lower atomic number elements were of interest and the main U component was already known[13]. The selected current minimized beam damage and ensured adequate count rate for EDS collection. Images and EDS were collected at either 10 or 15 kV with backscattered electron (BSE) signal and only images at 2 kV with both secondary (SE) and backscattered electron (BSE) signals were acquired to better understand the morphology and the atomic contrast distribution for each particle. Sample charging was observed when imaging, the scan rate and beam current setting were optimized to minimize this effect. Elemental maps were captured and quantified for each particle to display the distribution of the elements detected, with quantification done using the Bruker Esprit software option Q Map which include a 2 × 2 or 4 × 4 tile size to bin the pixels for better counting statistics and displayed results in normalized mass percent.

ICP-OES measurements were used to determine taggant concentrations in solid phase UNH, studtite, and metastudtite and are detailed in Table S1 (Supporting Information). Uranyl nitrate samples and a blank (untagged sample) of studtite were prepared by gravimetrically dissolving ~200 mg of material in ~50 mL of 8 M HNO_3 (Fisher Chemical, Optima grade). For tagged studtite, less material was available relative to UNH and the studtite blank, so ~30 mL of 8 M HNO_3 was introduced to ~90 mg of sample in Teflon digestion vessels. Likewise, ~60 mg of metastudtite samples were digested with 8 M HNO_3. Owing to the low solubility of studtite and metastudtite, these samples (after addition of HNO_3) were heated on a hotplate at 100 °C for 72 h prior to matrix removal and analysis. U matrix removal was done via a Uranium and

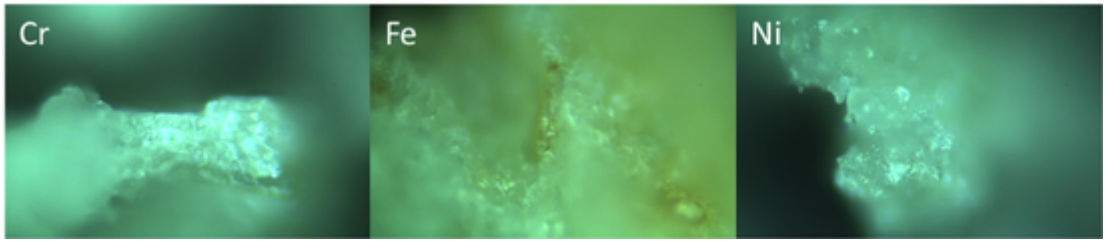

Fig. 1. Uranyl nitrate samples prepared with Cr, Fe, and Ni. Horizontal field of view for each image is 150 μm.

TEtra VAlent (UTEVA, Eichrom) ion exchange resin with an automated separation system (micro*FAST* MC, Elemental Scientific Inc., ESI, Omaha, NE). This automated separation procedure, developed by Manard et al., has been previously described in detail[14,15]. Quality control samples (certified reference material 124–1 [16], New Brunswick Laboratory Program Office, Argonne, IL; CUP-2[17], Canadian Uranium Product, Ottawa, Canada) were employed for analysis validation. After separation, the fractions were collected, diluted to 4 M HNO_3, and quantified via external calibration with an iCAP PRO (Thermo Scientific, Bremen, Germany) ICP-OES. Samples were introduced utilizing an Elemental Scientific Inc. (ESI, Omaha, NE, USA) SC-2DXi autosampler into a quartz nebulizer housed within a quartz spray chamber. The ICP-OES is equipped with a simultaneous echelle spectrometer and a high-speed charge injection device (CID) detector for the simultaneous detection of all wavelengths (167 – 852 nm). All samples and quality control samples were prepared with gravimetric quantification using external calibration with multi-element standards (High Purity Standards, Charleston, SC, USA). Measurement uncertainty was determined with an expanded uncertainty approach utilizing components such as analysis uncertainty, calibration uncertainty, and quality control uncertainty based on calculations from triplicate measurements of digested samples.

3. Results

3.1. Tagged uranyl nitrate

Zero shift corrected powder X-ray diffractograms for uranyl nitrate prepared as described in the materials and methods section are shown in Fig. 2. PXRD data are in excellent agreement with reflections simulated from published experimental single crystal X-ray diffraction data (Inorganic Crystal Structure Database Collection Code 23,814). When comparing the blank (untagged) uranyl nitrate hexahydrate to the expected pattern, only slight differences are observed in reflection intensity with all calculated reflections represented in the experimental data. Higher intensities are observed for the (112) and (202) reflections in the experimental data for untagged uranyl nitrate relative to calculated intensities. The same increased intensity of the (112) and (202) reflections is seen in Cr, Fe, and Ni-tagged uranyl nitrate, suggesting that the higher electron density observed for these reflections with PXRD is unrelated to taggant incorporation, rather, it is a function of preferred orientation or similar measurement-related effect.

Uranyl nitrate tagged with Fe shows a striking addition to the powder diffractogram, with a high-intensity doublet of Bragg peaks located at 41.02 and 41.14° 2θ. Reflections for uranyl nitrate are expected in this region, with the (224) and (600) appearing at 41° 2θ. However, the observed intensity for these reflections is higher than that of the (200), which is predicted to have the highest intensity. Attempts to map this pair of reflections to a secondary phase were unsuccessful. We hypothesize that the origin of this observed intensity is related to a slight shift in the coordinates of U sites within the uranyl nitrate structure and subsequent accommodation of Fe within the (600) plane. Scrutinization of the diffractogram obtained for Ni-doped uranyl nitrate in the range of 14–16° 2θ reveals potential additional complexity, with possible splitting of the (002) observed. A reduction of symmetry to accommodate Ni atoms in interstices between uranyl nitrate coordination units is plausible. No significant differences in the Cr-doped uranyl nitrate are observed when compared to untagged material.

Raman spectra collected for untagged uranyl nitrate prepared during this work are shown in Fig. 3a with vibrational mode assignments from Ohwada [18]. Like observations from PXRD for tagged uranyl nitrate, excellent agreement is observed between the spectra tagged and untagged samples. Closer examination of the low energy region, between ~50 and 250 cm^{-1} (Fig. 3b) reveals intensity differences between collected spectra. Likewise, the high-energy region of the spectra shows considerable variability in the intensity, bandwidth, and high-energy shoulder features in ν_2 NO_3^- modes (Fig. 3c).

To explore structural influences of taggant incorporation in more detail, we conducted two separate analyses of collected Raman spectra. First, we quantitatively compare the spectra of tagged and untagged UNH using a simple linear regression method (Fig. 4). Then, we examined difference spectra for the tagged UNH phases to understand potential mechanisms that govern taggant incorporation (Fig. 5). For linear regression analysis, we first normalize all collected spectra to total

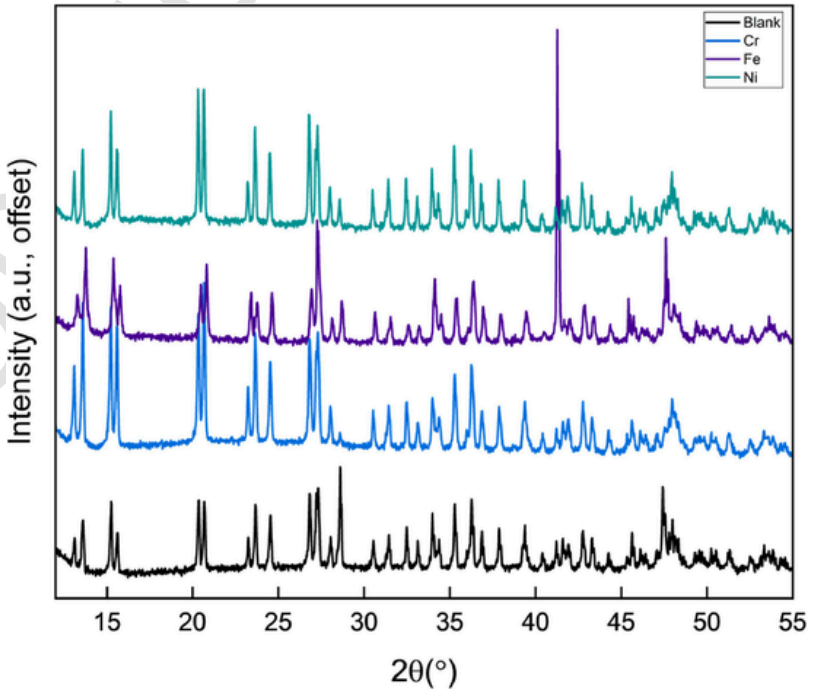

Fig. 2. Zero shift corrected powder X-ray diffractograms for uranyl nitrate samples. The (111) and (220) reflections of NIST 640e are visible at 28.441 and 47.300 ° 2θ, respectively. Diffractograms are offset for visibility.

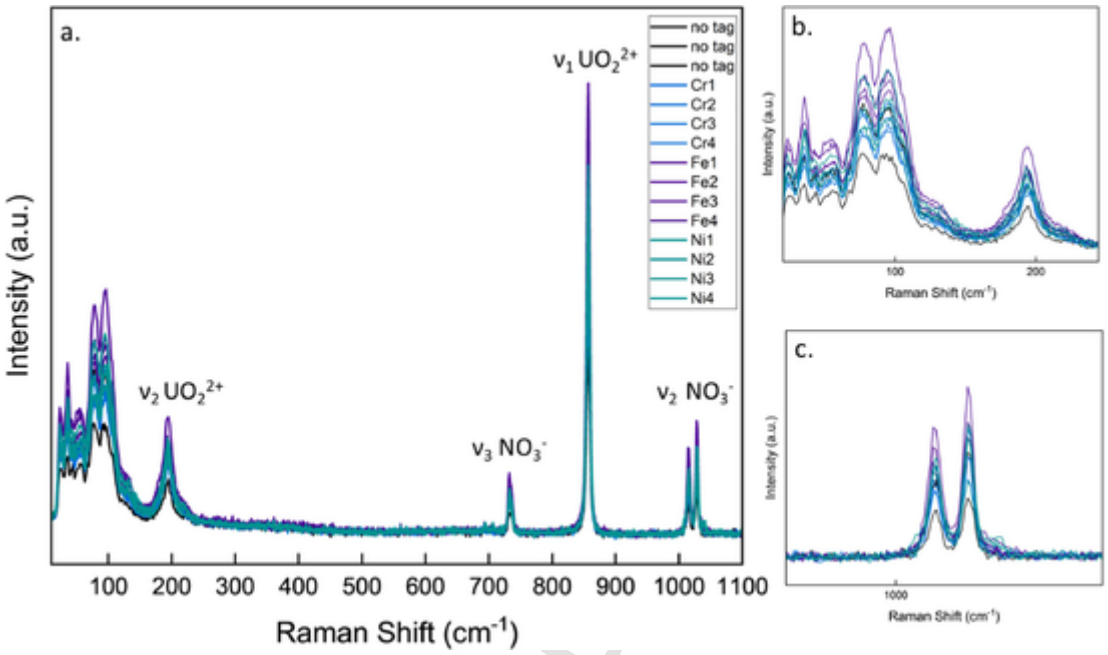

Fig. 3. a. Raman spectra collected for tagged and untagged samples of uranyl nitrate. b. The low energy region of uranyl nitrate Raman spectra. c. The high energy region of uranyl nitrate Raman spectra.

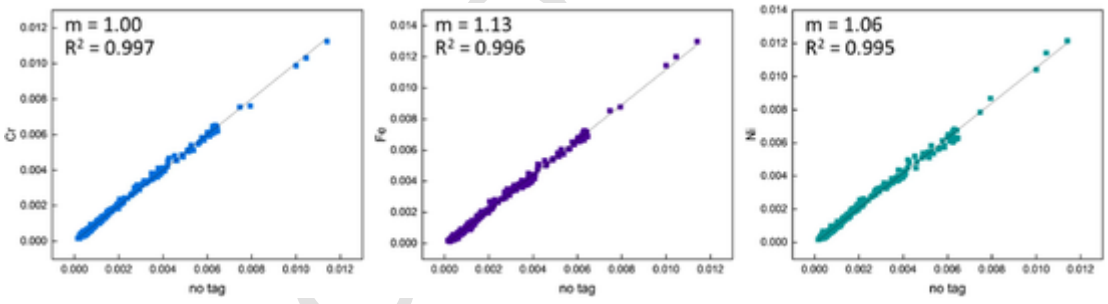

Fig. 4. Linear regression results for the average, normalized intensity of Cr, Fe, and Ni tagged uranyl nitrate spectra compared to the average, normalized intensity of untagged uranyl nitrate spectra.

counts, resulting in data on identical intensity scales. Second, average spectra are calculated for blank uranyl nitrate, and each of the tagged samples. For example, in Fig. 3, several spectra for each variety of uranyl nitrate are shown. To facilitate comparison, intensities at each wavenumber increment are summed and then divided by the number of spectra included. In the case of untagged UNH, for example, this involved summing the three collected spectra, and dividing by three to obtain the average spectrum. Following average spectra determinations, the intensity at each datapoint for tagged UNH samples are plotted as a function of the intensity at the same point in the average spectrum of untagged UNH. If the spectra of tagged and untagged uranyl nitrate are identical, linear regression of these biplots should result in a slope and correlation coefficient of 1. Indeed, slopes of 1.13, 1.00, and 1.06 are observed for Fe, Cr, and Ni-doped uranyl nitrate, respectively, when compared with untagged uranyl nitrate. Although we cannot determine the origin of spectral deviations observed for Fe-tagged UNH definitively, differences in signal intensity are observed and agrees with observations from PXRD where the diffractogram of the Fe sample also shows significant differences in the intensity of some reflections that could indicate taggant incorporation or precipitation of a secondary mixed Fe/U nitrate phase.

Utilizing the intensity-normalized average spectrum for untagged uranyl nitrate, we computed difference spectra by subtracting the average uranyl nitrate spectrum from each spectrum collected for tagged uranyl nitrate (Fig. 5). In general, increases in intensity are observed for the Fe-tagged samples, particularly in the regions where UO_2^{2+} translational (~100 cm^{-1}) and UO_2^{2+} symmetric stretching (~855 cm^{-1}) modes appear. Ni and Fe-tagged UNH both show higher intensity in ν_2 UO_2^{2+}, ν_3 $NO_3^-$and ν_2 NO_3^-modes, located at ~200, 750, and 1100 cm^{-1}, respectively. In contrast, UNH tagged with Cr shows lower intensity upon examination of difference spectra.

Taggant incorporation and potential secondary phase precipitation was further examined using SEM-EDS. Fe doped uranyl nitrate maps were collected at a lower accelerating voltage relative to those obtained for untagged UNH (see supporting information). The Fe-UNH sample was prone to beam damage and particle distortion at the higher kV. SEM-EDS results show that Fe is not homogenously mixed with the uranyl nitrate but instead forms a separate layer underneath the uranyl nitrate in flakes. UNH also appears as occlusions on the surface of Fe-rich particles (e.g., Fig. 6). Therefore, we hypothesize that two phases of uranyl nitrate are present, Fe-rich, and Fe-poor that are perhaps responsible for observed differences in Raman spectra for Fe-UNH compared to the untagged sample during linear regression and difference spectra analysis. Cr was found in either trace amounts or not visually present via inspection of the spectra, however, Fig. 7 shows relatively homogeneous co-location of Cr and U signal, suggesting that Cr incorporation may be occurring in UNH. Results from Raman spectroscopy and PXRD for Cr-UNH displayed limited structural perturbations, fur-

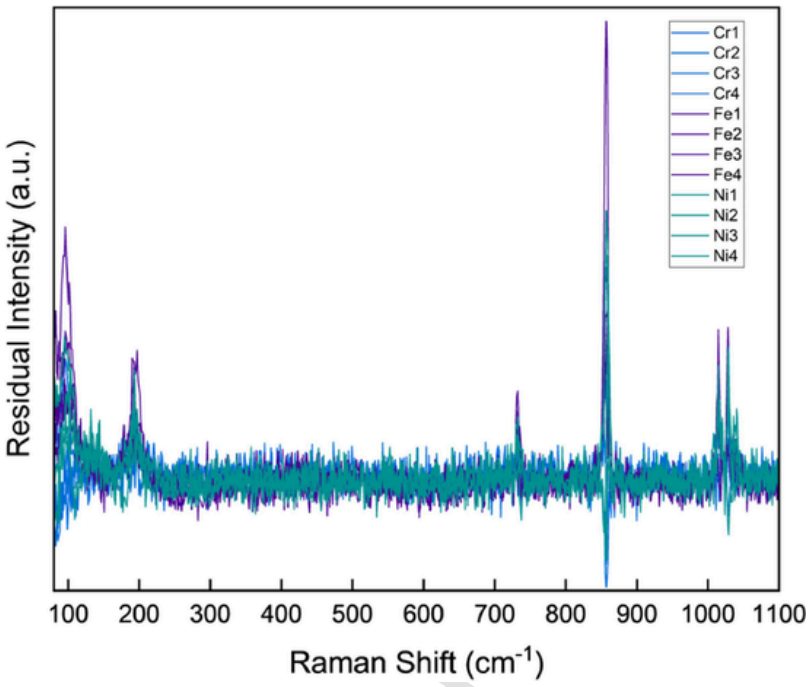

Fig. 5. Difference spectra for Cr, Fe, and Ni tagged uranyl nitrate.

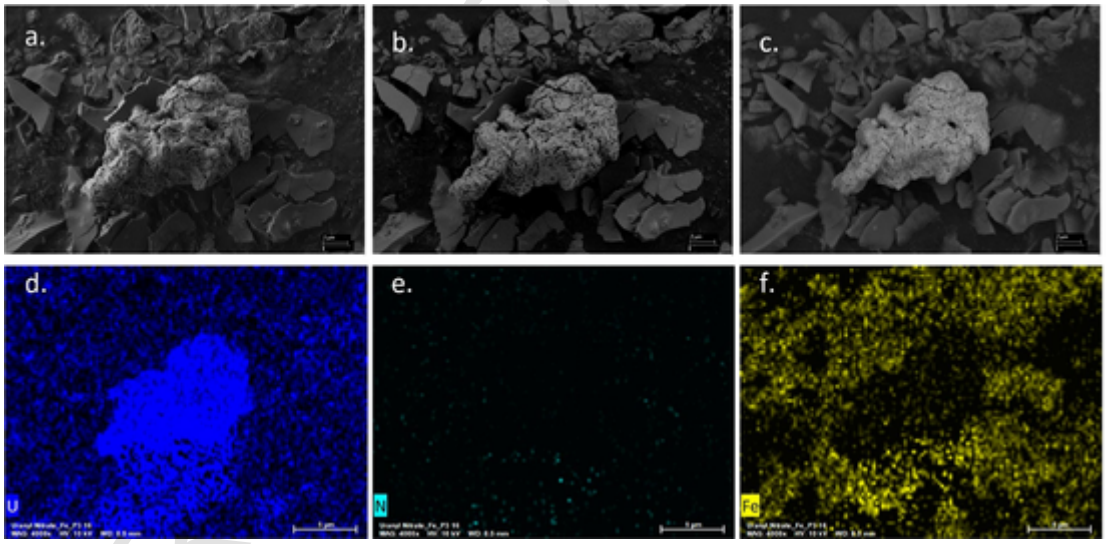

Fig. 6. Secondary and backscatter electron images and elemental maps collected for Fe-tagged uranyl nitrate a. Secondary electron (SE) image at 2 kV, b. Backscatter electron (BSE) image at 2 kV, c. BSE at 10 kV. d. Normalized weight% U map e. Normalized weight% N map f. Normalized weight% Fe map.

ther indicating that incorporation of Cr may be successful. The BSE image mode was used extensively to locate particles that demonstrated areas with darker contrast to analyze. The Ni-tagged UNH followed similar mixing properties as the other taggants, with both separate phases and colocation of Ni and U (and potential incorporation) suggested by results show in Fig. 8 rather than homogenous incorporation. ICP-OES measurements (Supporting Information, Table S1) indicate that taggants are present in solid phase UNH samples, with varying levels of incorporation. CrUNH contains ~2732 ug g^{-1} Cr, FeUNH appears to have lower taggant concentration, ~2000 ug g^{-1}, and NiUNH displays the lowest taggant concentration, ~1343 ug g^{-1}. From these results and our synthesis conditions, complete taggant incorporation is observed for the Cr sample, whereas taggant concentrations for Ni and FeUNH are lower than expected.

3.2. *Tagged studtite*

PXRD data for synthesized studtite are shown in Fig. 9. Excellent agreement between tagged and untagged studtite synthesized in this work is observed. Slight shifts (~0.07° 2θ) in the (200) (110) doublet are observed when comparing samples prepared with Cr and Fe to untagged and Ni studtite. No additional deviations compared to the tagged and untagged samples are seen, with all expected reflections visible, and no additional peaks that would indicate the presence of a secondary phase. We note that there are perhaps some contributions to the diffractogram of Ni-studtite from an amorphous phase, indicated by slightly higher background beginning at ~25 °2θ[19].

Raman spectra collected for studtite samples prepared during this work are shown in Fig. 10 with vibrational mode assignments from Colmenero et al. [20] Optical images of the specimens examined are

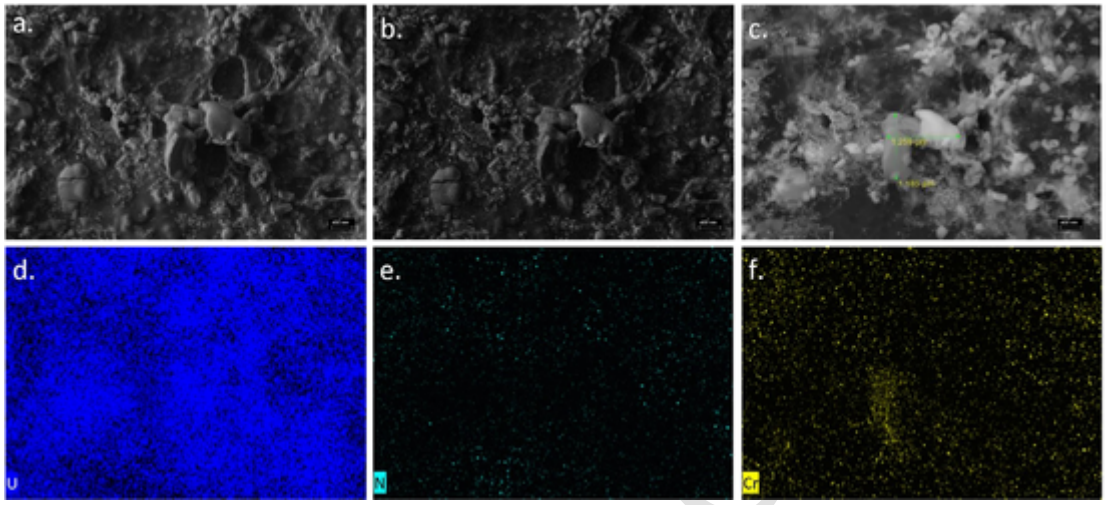

Fig. 7. Secondary and backscatter electron images and elemental maps collected for Cr-tagged uranyl nitrate a. Secondary electron (SE) image at 2 kV, b. Backscatter electron (BSE) image at 2 kV, c. BSE at 10 kV. d. Normalized weight% U map e. Normalized weight% N map f. Normalized weight% Cr map.

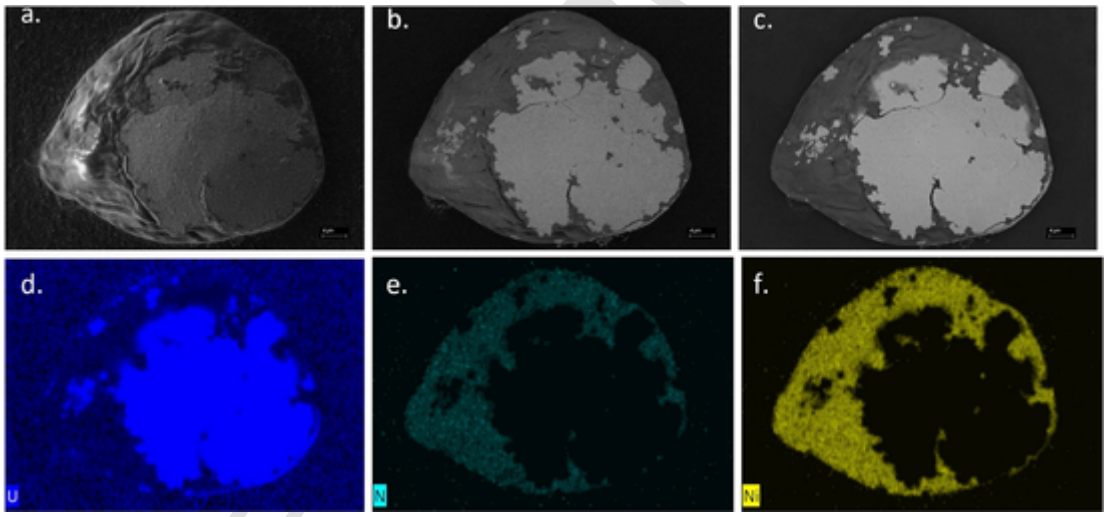

Fig. 8. Secondary and backscatter electron images and elemental maps collected for Ni-tagged uranyl nitrate a. Secondary electron (SE) image at 2 kV, b. Backscatter electron (BSE) image at 2 kV, c. BSE at 10 kV. d. Normalized weight% U map e. Normalized weight% N map f. Normalized weight% Ni map.

shown in Fig. 11. Like observations from PXRD, excellent agreement is observed upon visual comparison of Raman spectra of tagged and untagged studtite samples. Using the same techniques for more quantitative analysis of Raman spectra described in Section 3.1, which include linear regression and difference spectra, we see strong agreement between intensity normalized Raman spectra of tagged and untagged samples (Fig. 12). Slopes of 0.99, 0.99, and 1.09 are observed for Fe, Cr, and Ni-doped studtite, respectively. These results suggest that the Raman spectrum of Ni-studtite has a slightly higher intensity than the untagged sample, which is consistent with visual examination of Fig. 10. Of note, correlation coefficients of 0.999 are seen for all three samples compared to untagged studtite. Fig. 13 shows difference spectra computed for intensity-normalized spectra of tagged studtite compared to the untagged sample prepared in this work. The intensity differences between Ni and untagged studtite noted during our linear regression is evident here, with significantly higher intensity observed in the region of U-O_{eq} combination bands, and $\nu_1UO_2^{2+}$ and ν_1OO vibrational modes relative to the untagged samples. Conversely, significantly lower Raman signal is observed between the Cr studtite and untagged sample in the same regions of the spectra, while Fe studtite has slightly lower Raman signal in the vibrational mode located at ~136 cm^{-1}. There appears to be closer agreement between the intensity of Fe studtite and the untagged sample. Examination of the difference spectra suggests that peak shifts or asymmetry may be present for the Fe-sample as indicated by the negative intensity centered at 817 cm^{-1}, and positive intensity at slightly higher energy, 828 cm^{-1}.

EDS maps detect only trace amounts of each taggant in association with studtite particles. By visual inspection, brightness had to be raised three times the highest peak to visually see taggants present in the spectra (e.g., Supporting Information Fig. S1). Tagged materials were more robust compared to untagged studtite and were able to withstand higher kV and were analyzed at 15 kV without particle distortion. Given the taggant sample robustness, colocation was evident despite low overall taggant concentrations in the tagged studtite material. Fe studtite shows evidence of U and Fe colocation (Fig. 14), although the distribution of Fe appears heterogeneous. Cr content of tagged studtite is low, but relatively homogenous dispersion of Cr is evidenced by EDS maps shown in Fig. 15. Like results for other tagged studtite samples, increasing acceleration voltage revealed areas of Ni intensity in tagged studtite (Fig. 16). ICP-OES measurements indicate low, but detectable taggant concentrations in studtite. For Cr, Fe, and Ni studtite, 281, 655, and 754 ug g^{-1} of each tag are observed in the solid phase, respectively (Supporting Information, Table S1).

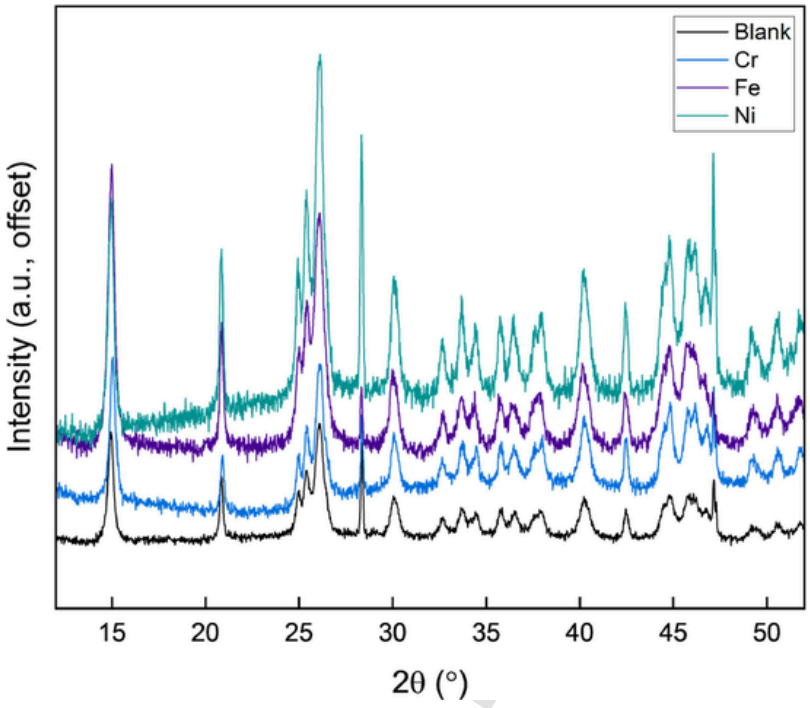

Fig. 9. Zero shift corrected powder X-ray diffractograms for studtite samples. The (111) and (220) reflections of NIST 640e are visible at 28.441 and 47.300 ° 2θ, respectively.

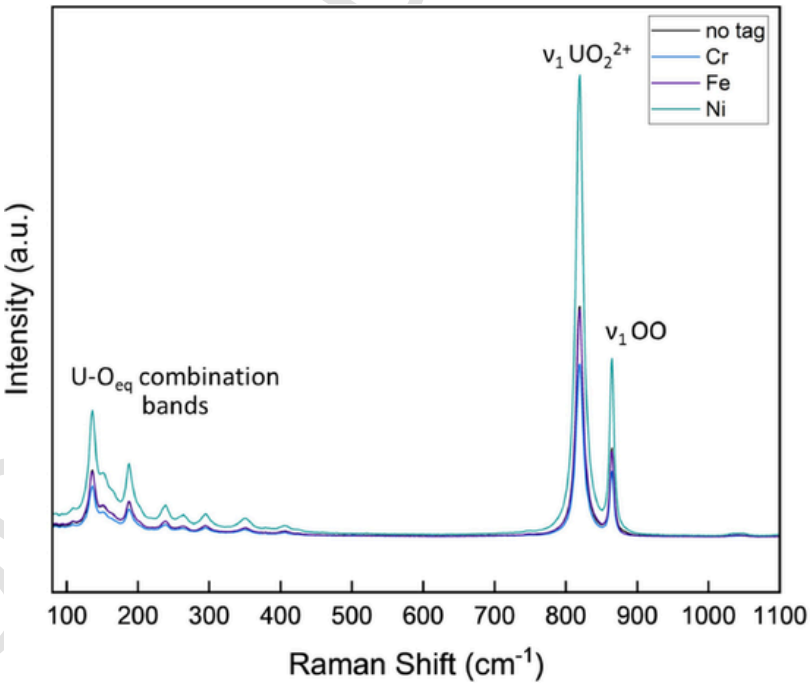

Fig. 10. Raman spectra collected for tagged and untagged samples of studtite.

3.3. Tagged metastudtite

Powder X-ray diffractograms collected for tagged metastudtite are in excellent agreement with data obtained for an untagged blank sample of metastudtite prepared at the same time as the tagged samples. All data show reflections that correspond with the expected diffraction pattern for metastudtite[12]. No additional reflections that would indicate the presence of a secondary phase are observed (Fig. 17).

Raman spectra collected for tagged and untagged metastudtite are shown in Fig. 18. Similar to observations from PXRD, all major vibrational modes are observed when comparing the Raman spectra of tagged and untagged metastudtite. A slight shift in the $\nu_1 UO_2^{2+}$ and $\nu_1 OO$ vibrational modes may be present for Ni- and Cr-metastudtite relative to the Fe and untagged samples, however, this shift of ~1 cm^{-1} is at the boundary of our instrument resolution. Intensity differences are present when comparing the low-wavenumber modes (lattice vibrations at ~154, 180, and 190 cm^{-1}) for the tagged samples to untagged

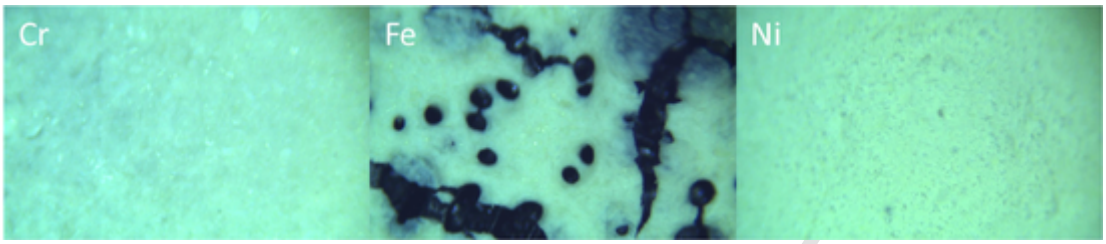

Fig. 11. Studtite samples prepared with Cr, Fe, and Ni. Horizontal field of view for each image is 150 μm.

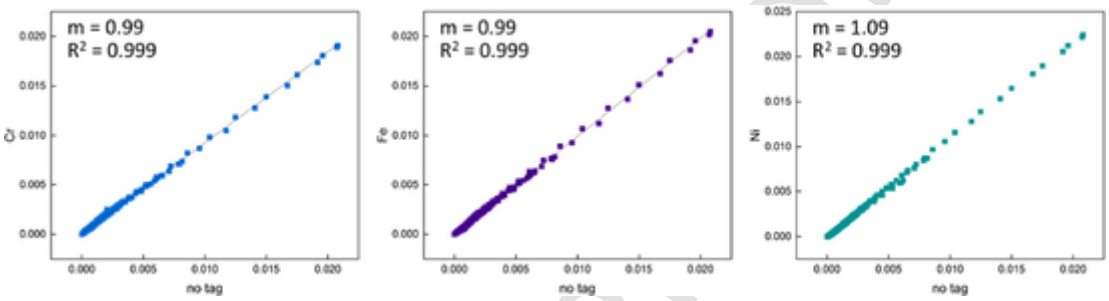

Fig. 12. Linear regression results for the average, normalized intensity of Cr, Fe, and Ni tagged studtite spectra compared to the average, normalized intensity of untagged studtite spectra.

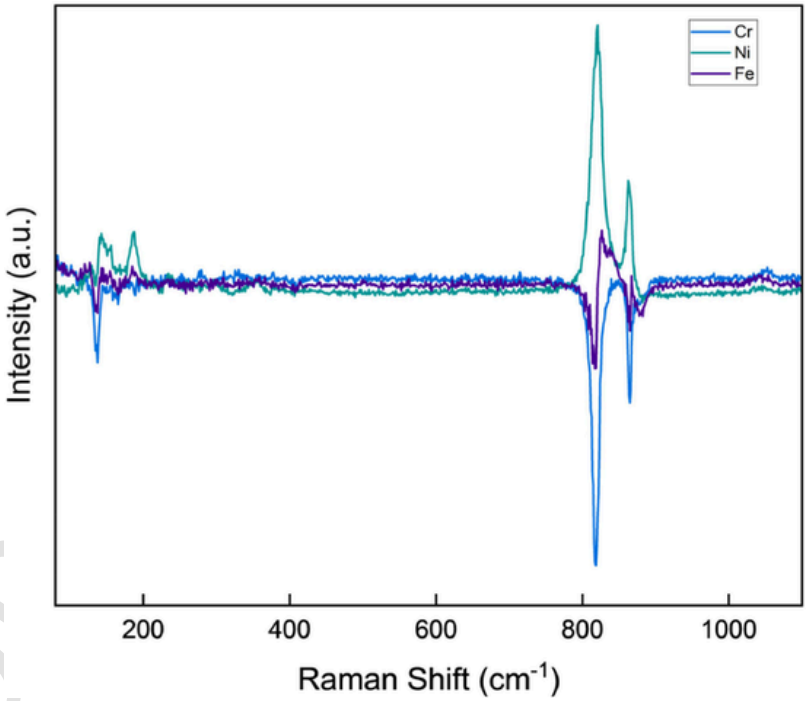

Fig. 13. Difference spectra for Cr, Fe, and Ni tagged studtite.

metastudtite. Differences in the observed intensity of modes in the region of 180–190 cm^{-1} for tagged metastudtite when compared to the untagged sample may be due to slight differences in hydrogen bonding networks present in the interstices of the metastudtite structure[12]. Following methods described for analysis and comparison of tagged and untagged uranyl nitrate and studtite in Section 3.1, we also investigated the difference in spectra for Cr, Fe, and Ni-metastudtite (Fig. 19). Using this method, variability is observed between the position of low-energy modes in Fe-metastudtite. In particular, modes between ~100 and 400 cm^{-1} in Fe-metastudtite are shifted to higher energy relative to Ni and Cr-metastudtite. Shifts in position and intensity of $\nu_1UO_2^{2+}$ and ν_1OO vibrational modes are also observed for tagged metastudtite samples [12,20]. While Fe and Ni are in relatively good agreement with the untagged sample as evidenced by primarily positive intensity suggesting only differences in intensity, negative intensity observed for Cr metastudtite here suggests that there is a slight shift in the $\nu_1UO_2^{2+}$ and ν_1OO modes of this sample to lower energy. The intensity differences observed in overlays of intensity-normalized and difference-spectra seen during comparison of tagged and untagged metastudtite are further confirmed by results of linear regression of average spectra of untagged metastudtite compared with Fe, Cr, and Ni samples (Fig. 20). Slopes of 0.83, 0.90, and 0.77 are observed for Fe, Cr, and Ni metastudtite respectively, were calculated from linear regression results. While correlation coefficients remain relatively stable (0.998 Fe, 0.990

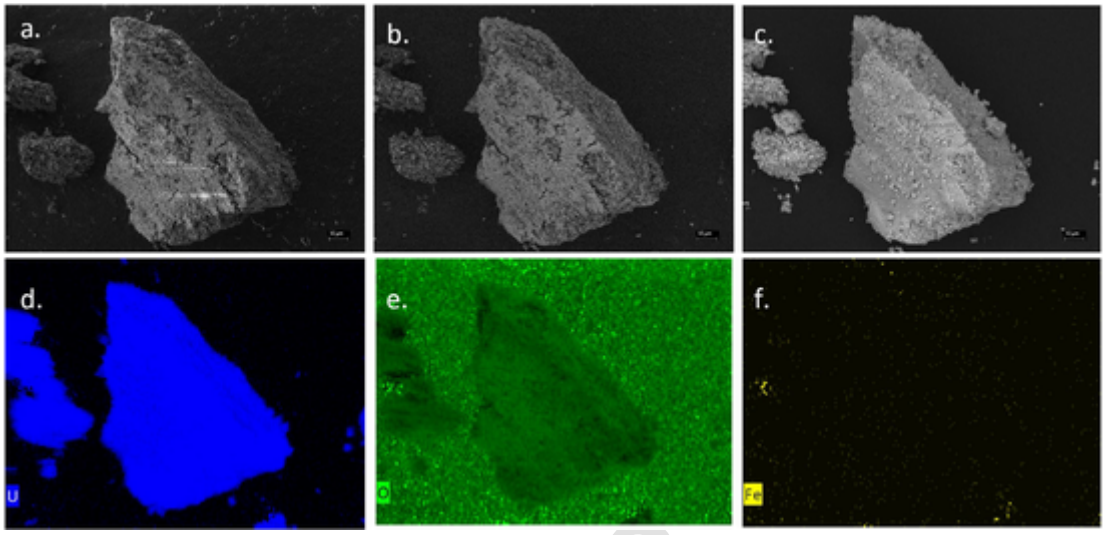

Fig. 14. Secondary and backscatter electron images and elemental maps collected for Fe-tagged studtite. Secondary electron (SE) image at 2 kV, b. Backscatter electron (BSE) image at 2 kV, c. BSE at 10 kV. d. Normalized weight% U map e. Normalized weight% N map f. Normalized weight% Fe map.

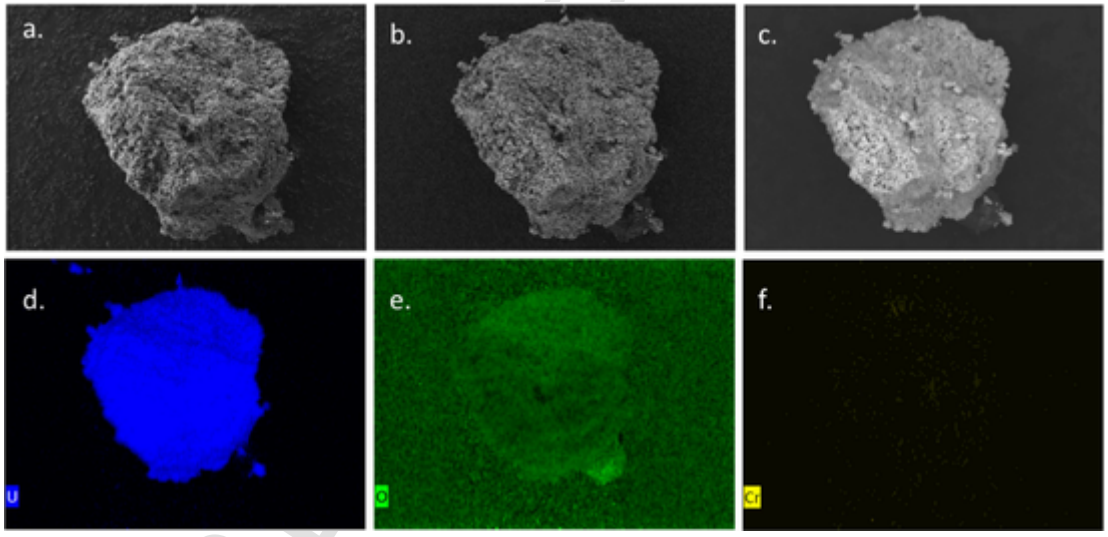

Fig. 15. Secondary and backscatter electron images and elemental maps collected for Cr-tagged studtite. Secondary electron (SE) image at 2 kV, b. Backscatter electron (BSE) image at 2 kV, c. BSE at 10 kV, d. Normalized weight% U map, e. Normalized weight% N map f. Normalized weight% Cr map.

Cr, and 0.991 Ni), these results suggest that there are taggant influences on the observed Raman spectra of metastudtite.

Based on images and EDS maps for metastudtite, this phase appears to react to the electron beam similarly to studtite. The samples are robust enough to withstand 15 kV and Fe concentrations, although low, appear to coincide with U (Fig. 21). Ni and Cr taggants however, are primarily observed in higher concentrations as fiber-like particles with the uranium adhered to it (Figs. 22 and 23). A line scan collected for the fiber-like particle shows low z material containing Cr or Ni and bright regions as predominately uranium (see supporting information). These results suggest that segregation of taggant species into secondary phases may occur during the thermal treatment of studtite used to form metastudtite.

As one may expect from dehydration, higher taggant concentrations are observed from ICP-OES in metastudtite relative to studtite. ~912, 966, and 290 ug g^{-1} of Cr, Fe, and Ni in the solid phase, respectively were determined for tagged studtite samples (Supporting Information, Table S1).

4. Discussion

Observations from SEM images and EDS spectral maps show that tagged uranyl nitrate forms separate phases rather than mixing with the uranyl nitrate matrix, whether as an occlusion or in trace amounts that were not able to be detected within the primary phase. Only one of the tagged uranyl nitrate samples showed distinct evidence that a secondary phase may be present from PXRD, and no secondary phases were observed from Raman spectroscopy. Although we attempted to gain an understanding of the overall concentration of taggants in the solid phase by ICP-OES, the heterogenous distribution, and possible secondary phase precipitation likely led to the observed discrepancies between expected (from synthesis conditions) maximum and actual (measured with ICP-OES) taggant concentrations, as our total tagged uranyl nitrate samples were ~10 g of material, and we only digested 200 mg of material for ICP-OES measurements. While the concentration of Cr in CrUNH was within the expected range for complete taggant incorporation, the relatively low incorporation indicated by ICP-OES for Fe and Ni may be the result of sampling a portion of solid phase

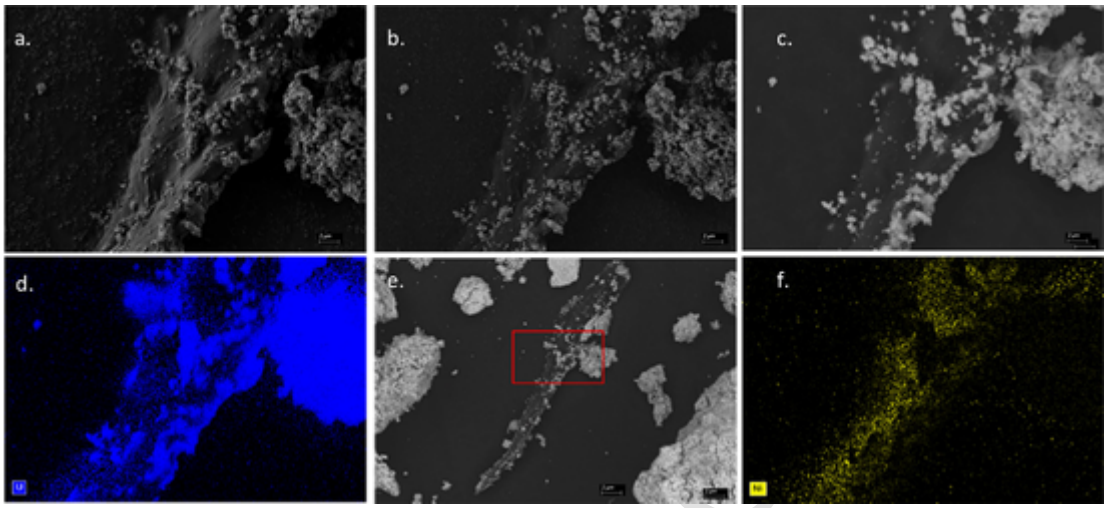

Fig. 16. Secondary and backscatter electron images and elemental maps collected for Ni-tagged studtite. a. Secondary electron (SE) image at 2 kV, b. Backscatter electron (BSE) image at 2 kV, c. BSE at 15 kV. d. Normalized weight% U map, e. Location image, f. Normalized wt% Ni map.

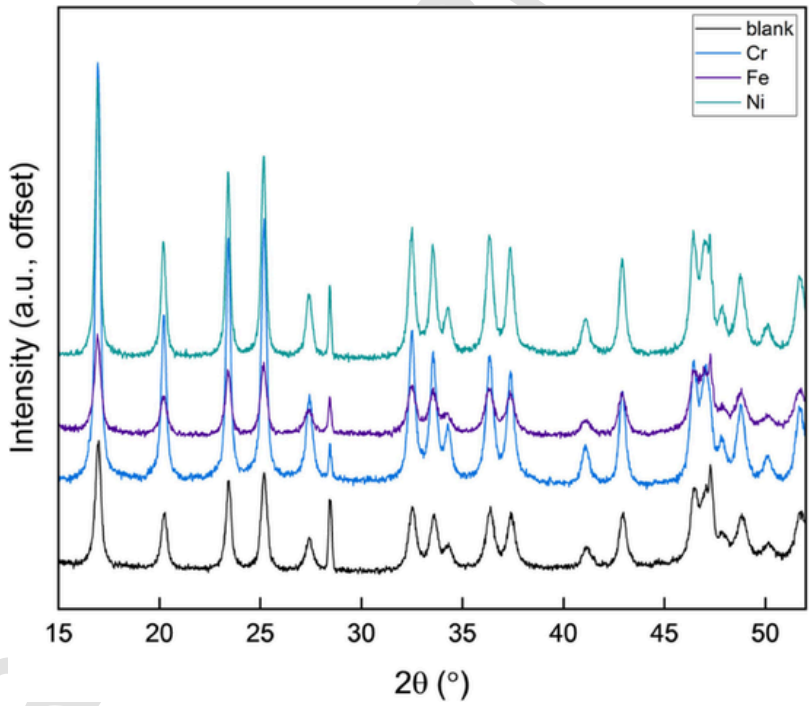

Fig. 17. Zero shift corrected powder X-ray diffractograms for metastudtite samples. The (111) and (220) reflections of NIST 640e are visible at 28.441 and 47.300 ° 2θ, respectively.

uranyl nitrate that did not have abundant co-precipitation of the taggant phases (e.g., see Fig. 8).

While limited homogeneous taggant incorporation was observed for uranyl nitrate phases, incorporation in studtite in low concentrations may be possible based on our analyses. This incorporation behavior could be attributable to the limited solubility and resulting rapid precipitation of studtite from tagged uranyl nitrate solutions[21]. While crystallization attempts for tagged UNH required slow evaporation, upon addition of H_2O_2 to aqueous uranyl nitrate solutions, studtite immediately precipitates, perhaps leading to the observed SEM-EDS results that suggest low-concentration taggant incorporation for Cr, Fe, and Ni (Fig. 14-16). Albeit low, taggant concentrations were still detectable using ICP-OES. These potential low-concentration incorporations are consistent with limited structural perturbations observed for tagged studtite compared to untagged studtite using PXRD and Raman spectroscopy. Slight perturbations in the (110) reflection of studtite are observed from PXRD, suggesting that slight contraction of axial U-O bonds may be a possible incorporation mechanism for transition metal tags in studtite [11]. This hypothesis is further supported by analysis of slight differences in frequency observed for the $\nu_1 UO_2^{2+}$ vibrational mode. Based on the relationship between vibrational frequency and uranyl bond length established by Bartlett and Cooney, a U-O bond of 1.7913 Å is calculated for untagged studtite, whereas tagged samples have a calculated U-O bond length of 1.7910 Å [22]. Additional studies beyond the scope of this work, including density functional theory investigations may provide additional insight into the incorporation mechanism of transition metal taggants in studtite.

SEM-EDS results indicate that some taggant species may be segregated from the main U phase in metastudtite, perhaps as a consequence of calcination from studtite, wherein loss of two loosely-bound water

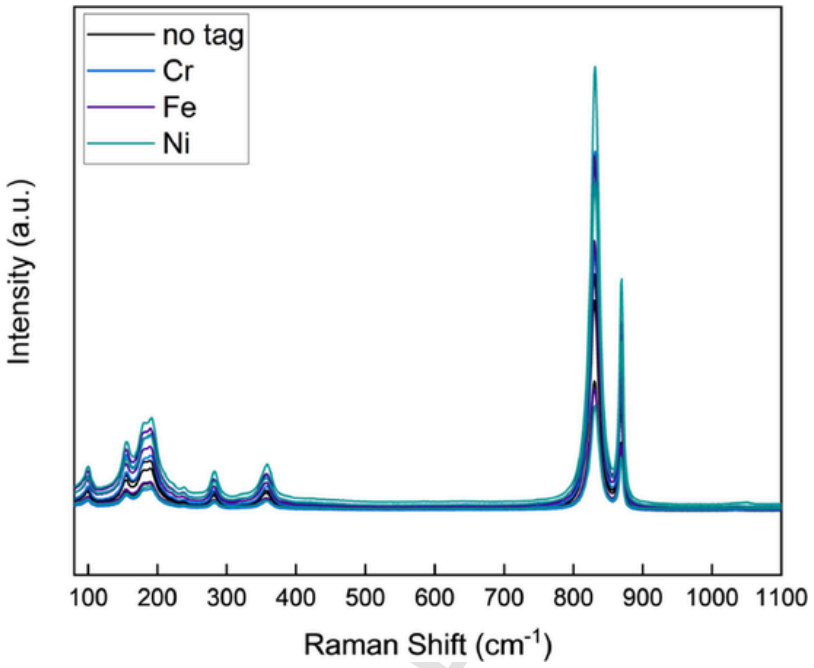

Fig. 18. Raman spectra collected for tagged and untagged samples of metastudtite.

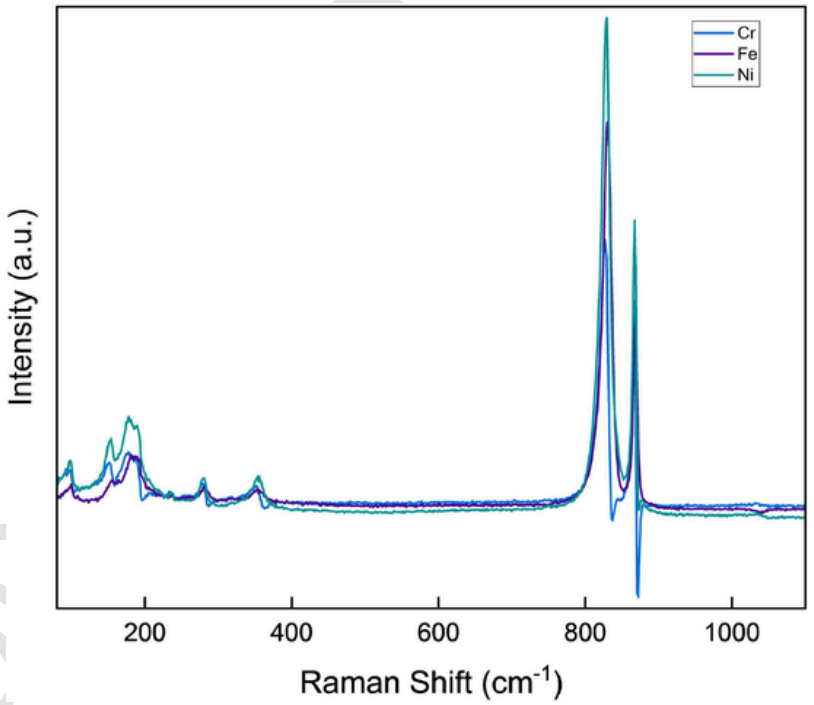

Fig. 19. Difference spectra for Cr, Fe, and Ni tagged metastudtite.

molecules may result in decreased stability and exsolution of taggants incorporated in the precursor. Loss of these two water molecules during calcination is also a likely cause of the higher concentrations of taggant observed in metastudtite samples from ICP-OES, combined with heterogeneous bulk samples as was seen for tagged UNH samples. Because the transition from studtite to metastudtite occurs in the solid state, a lower molecular mass for the calcination product would result in higher taggant concentration. Likewise, exsolution of taggants during heating is possible, resulting in long-range sample heterogeneity that could give rise to the observed elevated taggant concentrations in portions of tagged metastudtite implied by results from ICP-OES measurements.

Significant spectroscopic differences between tagged and untagged metastudtite are also observed for Cr and Ni studtite (Fig. 20). Despite the potential taggant segregation observed in metastudtite relative to studtite, initial incorporation of taggant species in studtite suggests that this is a plausible starting point for development of tagged higher oxides such as UO_3 or U_3O_8 that could be used to produce intentionally tagged UO_2.

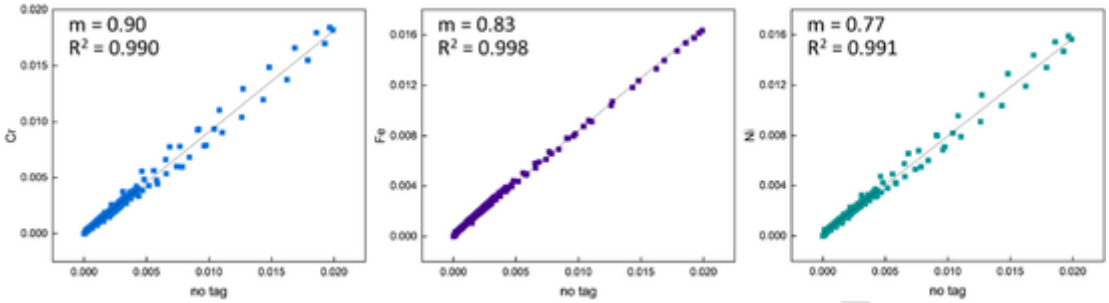

Fig. 20. Linear regression results for the average, normalized intensity of Cr, Fe, and Ni tagged studtite spectra compared to average, normalized intensity of untagged metastudtite spectra.

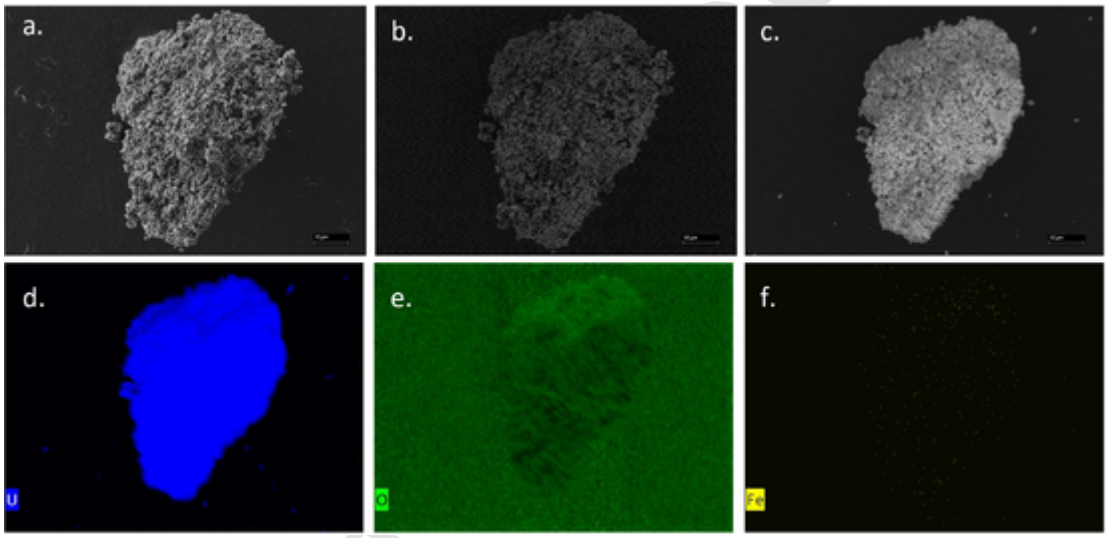

Fig. 21. Secondary and backscatter electron images and elemental maps collected for Fe-tagged metastudtite. Secondary electron (SE) image at 2 kV, b. Backscatter electron (BSE) image at 2 kV, c. BSE at 15 kV, d. Normalized weight% U map, e. Normalized weight% O map, f. Normalized weight% Fe map.

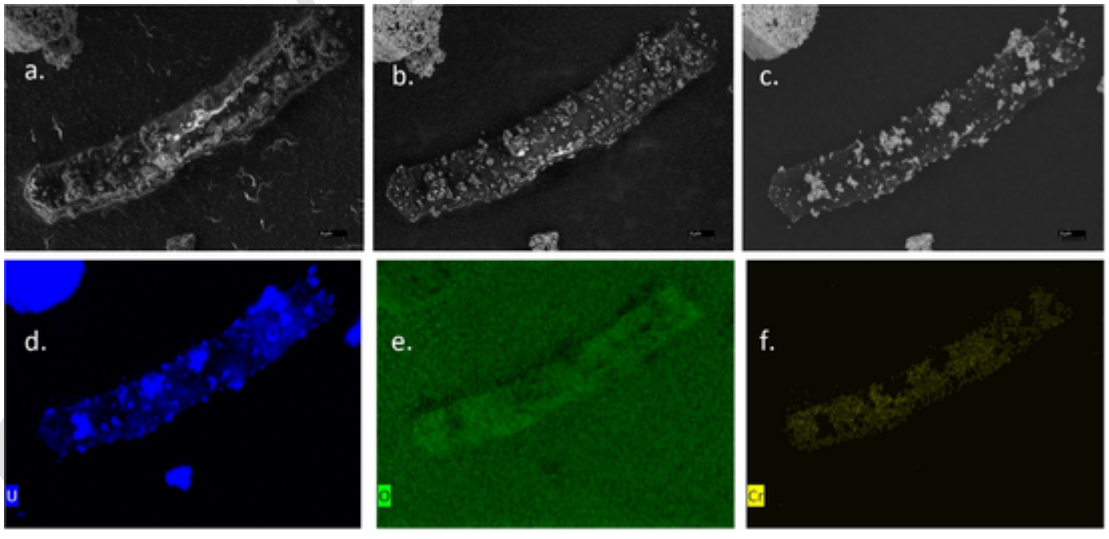

Fig. 22. Secondary and backscatter electron images and elemental maps collected for Cr-tagged metastudtite. Secondary electron (SE) image at 2 kV, b. Backscatter electron (BSE) image at 2 kV, c. BSE at 15 kV, d. Normalized weight% U map, e. Normalized weight% O map, f. Normalized weight% Cr map.

5. Conclusions

We explored structural features of Cr, Fe, and Ni taggant incorporation in uranyl nitrate, studtite, and metastudtite as a preliminary investigation into the plausibility of incorporating intentional forensic indicators in early nuclear fuel cycle materials. Using PXRD, we detect a potential secondary Fe-rich phase in uranyl nitrate that may have more complete taggant incorporation than the bulk uranyl nitrate precipitate. Secondary phases are not observed from PXRD for Cr and Ni UNH. Raman spectroscopic results for tagged uranyl nitrate are consistent

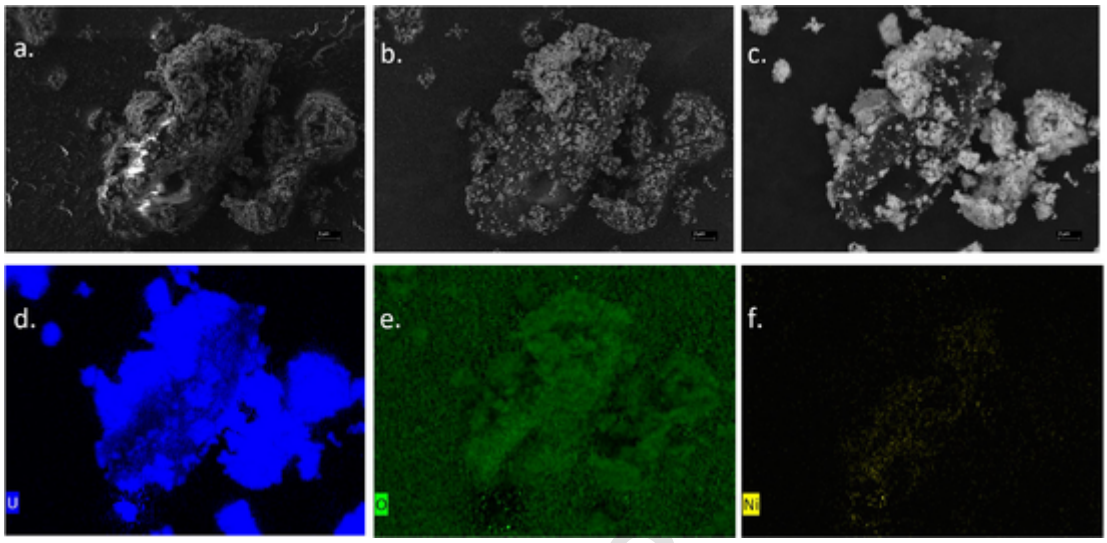

Fig. 23. Secondary and backscatter electron images and elemental maps collected for Cr-tagged metastudtite. Secondary electron (SE) image at 2 kV, b. Backscatter electron (BSE) image at 2 kV, c. BSE at 15 kV, d. Normalized weight% U map, e. Normalized weight% O map, f. Normalized weight% Cr map.

with those of PXRD, where the largest differences between tagged and untagged sample spectra are observed for FeUNH. SEM-EDS results also confirm that taggant incorporation into uranyl nitrate is limited, with distinct secondary phases observed for Fe and Cr that are, nevertheless, co-located with U. Colocation of U and Ni from SEM-EDS suggests that this transition metal is the most likely to incorporate in uranyl nitrate, but it remains unclear whether Ni is intercalated within the uranyl nitrate phase, or is a secondary phase that coprecipitates. Heterogeneity observed using SEM-EDS is also suggested by ICP-OES measurements.

Taggant incorporation in studtite is possible, either in the form of structurally incorporated transition metals, or perhaps as a minor secondary phase entrained within particles of studtite that rapidly precipitate from aqueous solution. Secondary phases are not seen with PXRD, and the only observable perturbations to the Raman spectra originate from slight shifts in the $\nu_1 UO_2^{2+}$ vibrational mode, which could be a result of structural accommodation of taggants. Similarly, slight shifts in the reflection corresponding to interplanar spacing of axial U-O may further indicate that this is a viable mechanism for intentionally incorporating tags in early fuel cycle materials. While it appears that taggants are not completely incorporated during studtite precipitation, the presence of Cr, Fe, and Ni is indicated by ICP-OES measurements, suggesting that this intermediate material is viable for intentional forensic tagging and may result in more homogeneous incorporation of taggants in U_3O_8 or UO_2.

SEM-EDS measurements of tagged metastudtite reveal segregation of taggant signal, suggesting that heating of studtite reduces the fidelity of taggant incorporation. However, no secondary phases are observed from PXRD measurements, indicating that studtite may still be a viable precursor for formation of tagged higher oxides.

This work represents a foundation toward understanding the incorporation of intentional tags in early fuel cycle nuclear materials for forensic applications. We show that coprecipitation of uranyl phases (UNH and studtite) with transition metal taggants is possible and provide insight into potential mechanisms of incorporation in these bulk phases. We also observe that exsolution of taggant species occurs during thermal treatment of studtite, resulting in potential taggant segregation in metastudtite. Our work also informs potential methods by which naturally occurring trace elemental constituents relating to the geologic origin of nuclear materials may incorporate or partition during various stages of early fuel cycle processes. While detailed investigations into direct incorporation of taggant species via oxide mixing prior to sintering UO_2 are ongoing, we have explored the possibility of introducing taggant species at the earliest stages of the nuclear fuel cycle. Our future work to this end will involve intermediate calcination of these precursors to uranium trioxide polymorphs and direct calcination to U_3O_8 and UO_2 as a means of understanding how the timing of taggant incorporation influences the performance and structure of sintered UO_2.

CRediT authorship contribution statement

Tyler L. Spano : Conceptualization, Methodology, Formal analysis, Validation, Investigation, Writing – original draft, Writing – review & editing, Visualization. **Toya Beiswenger :** Investigation, Formal analysis, Visualization, Writing – original draft, Writing – review & editing, Visualization. **Benjamin T. Manard :** Methodology, Investigation, Validation, Formal analysis, Writing – original draft, Writing – review & editing. **Tash L. Ulrich :** Writing – review & editing. **Rodney Hunt :** Resources, Writing – review & editing. **Andrew Miskowiec :** Resources, Supervision, Writing – review & editing. **Ashley E. Shields :** Conceptualization, Writing – review & editing, Supervision, Project administration, Funding acquisition.

Declaration of Competing Interest

The authors declare that they have no known competing financial interests or personal relationships that could have appeared to influence the work reported in this paper.

Acknowledgements

The authors thank Ali Moore, Tara Rose, JJ Quinn, and Keith Gilbert for their support. Our work was greatly improved by fruitful discussions and feedback from Drs. Connor Parker and Luke Sadergaski, and from the helpful suggestions provided by two anonymous reviewers. This work was funded by the United States Department of Energy National Nuclear Security Administration (NNSA) Office of Defense Nuclear Nonproliferation (DNN) Research and Development Forensics program.

Supplementary materials

Supplementary material associated with this article can be found, in the online version, at doi:10.1016/j.jnucmat.2023.154787.

References

[1] H.E. Frimmel, S. Schedel, H. Brätz, Uraninite chemistry as forensic tool for provenance analysis, Appl. Geochem. 48 (2014) 104–121.

[2] E. Keegan, M. Wallenius, K. Mayer, Z. Varga, G. Rasmussen, Attribution of uranium ore concentrates using elemental and anionic data, Appl. Geochem. 27 (8) (2012) 1600–1609.

[3] M.J. Kristo, A.M. Gaffney, N. Marks, K. Knight, W.S. Cassata, I.D. Hutcheon, Nuclear forensic science: analysis of nuclear material out of regulatory control, Annu. Rev. Earth Planet. Sci. 44 (LLNL–JRNL–683854) (2016).

[4] J. Mercadier, M. Cuney, P. Lach, M.C. Boiron, J. Bonhoure, A. Richard, M. Leisen, P. Kister, Origin of uranium deposits revealed by their rare earth element signature, Terra Nova 23 (4) (2011) 264–269.

[5] P. Alexandre, K. Kyser, D. Layton-Matthews, B. Joy, Y. Uvarova, Chemical compositions of natural uraninite, Can. Mineral. 53 (4) (2015) 595–622.

[6] Z. Varga, M. Wallenius, A. Nicholl, K. Mayer, Assessment of uranium inhomogeneity and isotope imaging for nuclear forensics, Spectroch. Acta Part B Atomic Spectrosc. 171 (2020) 105920.

[7] T.L. Spano, A. Simonetti, T. Wheeler, G. Carpenter, D. Freet, E. Balboni, C. Dorais, P.C. Burns, A novel nuclear forensic tool involving deposit type normalized rare earth element signatures, Terra Nova 29 (5) (2017) 294–305.

[8] T.L. Spano, A. Simonetti, E. Balboni, C. Dorais, P.C. Burns, Trace element and U isotope analysis of uraninite and ore concentrate: applications for nuclear forensic investigations, Appl. Geochem. 84 (2017) 277–285.

[9] T.L. Spano, A. Simonetti, L. Corcoran, P.A. Smith, S.R. Lewis, P.C. Burns, Comparative chemical and structural analyses of two uranium dioxide fuel pellets, J. Nuclear Mater. 518 (2019) 149–161.

[10] K.L. LeBlanc, K. Nadeau, J. Meija, L. Yang, P.A. Babay, M.A. Bavio, C. Boome, D. Chipley, R.S. Cristaldo Leguizamón, J. Denton, Collaborative study for certification of trace elements in uranium ore concentrate CRMs UCLO-1, UCHI-1, and UPER-1, J. Radioanal. Nucl. Chem. 331 (9) (2022) 4031–4045.

[11] P.C. Burns, K.A. Hughes, Studtite,$[(UO_2)(O_2)(H_2O)_2](H_2O)_2$: the first structure of a peroxide mineral, Am. Mineral. 88 (7) (2003) 1165–1168.

[12] T.L. Spano, J.L. Niedziela, A.E. Shields, J. McFarlane, A. Zirakparvar, Z. Brubaker, R.J. Kapsimalis, A. Miskowiec, Structural, spectroscopic, and kinetic insight into the heating rate dependence of studtite and metastudtite dehydration, The Journal of Physical Chemistry C 124 (49) (2020) 26699–26713.

[13] J.I. Goldstein, D.E. Newbury, J.R. Michael, N.W. Ritchie, J.H.J. Scott, D.C. Joy, Scanning Electron Microscopy and X-ray Microanalysis, Springer, 2017.

[14] E.M. Wylie, B.T. Manard, C.D. Quarles Jr, L.A. Meyers, N. Xu, An automated micro-separation system for the chromatographic removal of uranium matrix for trace element analysis by ICP-OES, Talanta 189 (2018) 24–30.

[15] B.T. Manard, D.A. Bostick, S.C. Metzger, B.W. Ticknor, N.A. Zirakparvar, K.T. Rogers, C.R. Hexel, Rapid and automated separation of uranium ore concentrates for trace element analysis by inductively coupled plasma–optical emission spectroscopy/triple quadrupole mass spectrometry, Spectroch Acta Part B Atomic Spectrosc. 179 (2021) 106097.

[16] S. Bürger, K. Mathew, P. Mason, U. Narayanan, Reference materials characterized for impurities in uranium matrices: an overview and re-evaluation of the NBL CRM 124 series, J. Radioanal. Nucl. Cheml 279 (2) (2009) 659–673.

[17] J.S. Denton, D.A. Bostick, S.F. Boulyga, J.A. Cunningham, I. Dimayuga, C.R. Hexel, J. Hiess, S.V. Jovanovic, P. Kaye, T. Kell, International interlaboratory compilation of trace element concentrations in the CUP-2 uranium ore concentrate standard, J. Radioanal. Nucl. Chem. (2022) 1–16.

[18] K. Ohwada, Raman spectroscopic studies of some uranyl nitrate complexes, J. Coord. Chem. 8 (1) (1978) 35–39.

[19] P.F. Weck, E. Kim, C.F. Jové-Colón, D.C. Sassani, Structures of uranyl peroxide hydrates: a first-principles study of studtite and metastudtite, Dalton Trans. 41 (32) (2012) 9748–9752.

[20] F. Colmenero, L.J. Bonales, J. Cobos, V. Timón, Study of the thermal stability of studtite by in situ Raman spectroscopy and DFT calculations, Spectrochim. Acta Part A: Molecular Biomolecul. Spectrosc. 174 (2017) 245–253.

[21] KA.H. Kubatko, K.B. Helean, A. Navrotsky, P.C. Burns, Stability of peroxide-containing uranyl minerals, Science 302 (5648) (2003) 1191–1193.

[22] J.R. Bartlett, R.P. Cooney, On the determination of uranium-oxygen bond lengths in dioxouranium (VI) compounds by Raman spectroscopy, J. Mol. Struct. 193 (1989) 295–300.